JMEPEG (2012) 21:865–876
DOI: 10.1007/s11665-011-9947-7

1059-9495/$19.00

Analysis of WC/Ni-Based Coatings Deposited by Controlled Short-Circuit MIG Welding

P. Vespa, P.T. Pinard, R. Gauvin, and M. Brochu

(Submitted November 10, 2010)

This study investigates the recently developed controlled short-circuit metal inert gas (CSC-MIG) welding system for depositing WC/Ni-based claddings on carbon steel substrates. WC/Ni-based coatings deposited by CSC-MIG were analyzed by optical light microscopy and scanning electron microscopy (SEM) equipped with energy dispersive spectroscopy (EDS) and electron backscatter diffraction (EBSD) capabilities. X-ray diffraction (XRD) and hardness measurements of depositions are also reported. The CSC-MIG welding system provides a significant amount of user control over the current waveform during welding and has lower heat input when compared with traditional MIG welding. Heat input for the analyzed coatings ranged from 10.1 to 108.7 J/mm. Metallurgically bonded coatings free from spatter and with 0.75% average porosity were produced. It was found that the detrimental decarburization of the WC particles seen in thermal spray systems does not occur when welding with the CSC-MIG. Precipitation of a reaction layer around the reinforcing phase was identified as WC; the average thickness of which increases from 3.8 to 7.2 μm for the low and high heat input condition, respectively. Precipitation of newly formed WC particles was observed; their size distribution increased from D_{50} of 2.4 μm in the low heat input weldment to 6.75 μm in the high heat input weldment. The level of dilution of the reinforcing phase increases significantly with heat input. The hardness of the deposited coatings decreases from 587 HV_{10} to 410 HV_{10} when the energy input was increased from 10.1 to 108.7 J/mm.

Keywords CSC-MIG, GMAW, hardfacing, MIG, tungsten carbide, welding

1. Introduction

Coatings and coating deposition techniques are investigated because of the economic drive to reduce wear of materials in many industrial sectors (Ref 1). Tungsten carbide (WC) is highly investigated as a reinforcing agent because it exhibits many desirable mechanical properties such as high hardness and superior wettability by molten metals compared with other carbides (Ref 2-4). The WC powder particles act as the hard phase while the alloying elements form a ductile binder material; together they form a metal matrix composite (MMCs) and are used to significantly increase the wear life of industrial tools (Ref 5-7).

There are several methods available for the application of wear resistant WC coatings. One of the most widely applied thermal spray deposition techniques in industry is the high velocity oxygen fuel (HVOF) process (Ref 8-10). One of the main drawbacks associated with HVOF is the decarburization of WC during spraying to form the brittle and less wear resistant W_2C phase (Ref 11). Another disadvantage of thermal spray techniques is that there is no permanent metallurgical bond formed between the individual hardfacing material splats or between the splats and the substrate. Consequently, a certain amount of porosity exists in the coating which, in addition to the lower intersplat strength, can lead to chipping, removal of WC particles, and premature breakdown of the wear resistant barrier (Ref 12). In addition, this technique requires large initial capital expenditure and can be quite costly to run (Ref 8, 13). As can be seen, several shortcomings in the HVOF process create a need for alternative coating deposition techniques.

Compared with thermal spray techniques, welding-based processes require significantly less capital expenditure and lower operating costs. In addition, they form a permanent metallurgical bond between the deposited material and the substrate. These advantages make them an interesting alternative to thermal spray processes. However, the main drawback of welding-based hardfacing techniques is the high heat inputs required for deposition which favor excessive dissolution of the reinforcing phase.

Recent developments in metal inert gas (MIG) welding techniques have allowed for better control of welding parameters and reduction of heat input during welding. A variation on the conventional MIG welding process allows for lower heat inputs and is thus attractive as a coating deposition technique which can reduce the dissolution of the reinforcing carbide phase. The controlled short-circuit MIG (CSC-MIG) welding system is a welding apparatus developed in the late 1990s to overcome several shortcomings associated with traditional MIG welding (Ref 14). Traditional MIG welding is known to have problems associated with material deposition and process stability (Ref 14). The CSC-MIG operates in conjunction with a process control system and fast reacting wire feed unit to modulate the electrode wire's position and speed to obtain an extremely stable process in which spatter is nearly eliminated

P. Vespa, P.T. Pinard, R. Gauvin, and **M. Brochu**, Department of Mining and Materials Engineering, McGill University, 3610 University St., Montreal, QC H3A 2B2, Canada. Contact e-mail: mathieu.brochu@mcgill.ca.

(Ref 13, 15). The CSC-MIG operates using the short-circuit deposition method and uses a control system that allows the user to set the arc length, arc time, current, and several other welding parameters. Conventional MIG welding heat inputs range from 0.5 to 3.0 kJ/mm, while the CSC-MIG outputs range from 0.01 to 0.11 kJ/mm when using a WC/Ni-based hardfacing electrode wire (Ref 15, 16).

This research was conducted to study the features and transformations in the microstructure with heat input for WC/Ni-based coatings deposited by the controlled short-circuiting MIG welding system. Results on the microstructure evolution, phase formation, particle dissolution, and coating hardness will be presented.

2. Materials and Methods

Tests were conducted using the CSC-MIG welding system manufactured by Jetline Engineering. This system consists of two parts. The first is the WF-9829 MIG torch assembly which contains an electrode wire drive system and torch. The second part is the 9829 CSC MIG weld process controller which uses a microprocessor to monitor and control the welding process parameters. The welder was mounted on a 3′ by 3′ Machitech CNC table with three translational degrees of freedom and the generator used to power the welding system was a Miller Electric XMT 350 CC/CV.

The welding tests were monitored using ARCAgent 3000P data acquisition system manufactured by IMPACT Welding. This system was used to monitor current, voltage, and gas flow rate at a sampling frequency of 10 kHz. Heat input calculations provided by the monitoring system use the average instantaneous power of sampled data. This is regarded as the most accurate method of calculating heat input when current and voltage vary significantly with time (Ref 15, 17).

CSC-MIG welding parameters selection was based on visual inspection of cracking, discontinuity, repeatability, and fusion to the basemetal. In addition, the use of the CSC-MIG process combined with the high-speed data acquisition system made it possible to achieve process stability by ensuring an even arc burning time and short-circuiting time and by the elimination of welding spatter (Ref 18).

A 1.6 mm cored electrode wire, PolyTung NiBWC, from Polymet Corporation (Cincinnati, OH, USA) was used to produce coatings. PolyTung NiBWC has a pure Ni sheath, is filled with a FeSiB powder and contains WC particles as a reinforcing agent. Full chemical composition of the cored electrode wire containing 38-45 wt.% WC particles, as stated by manufacturer, is shown in Table 1. Feedstock WC ranged between 45 and 200 μm in diameter with a mean particle diameter of 71 μm. The particle size distribution of the tungsten carbide, as determined with a Horiba LA-920 laser scattering particle size distribution analyzer, is shown in Fig. 1. Figure 2 shows a micrograph of the WC powder, from which it can be seen that the feedstock is composed of angular particles.

Table 1 Chemical composition of Ni-based, WC reinforced welding wire supplied by Polymet Corporation (Cincinnati, OH, USA)

Chemical composition, wt.%					
Si	**B**	**Fe**	**C**	**W**	**Ni**
2.81	1.06	0.7	2.81	41.02	Balance

In these experiments, single bead weld deposits were made in the flat position at a 90° angle to the substrate. Welding was carried out at 1 meter per minute (mpm) on plain carbon steel plates having dimensions 100 × 12 × 2.5 mm. The steel substrate was sandblasted to remove surface impurities prior to welding. A 75Ar-25CO_2 shielding gas was used and flowed between 36 and 37 cubic meters per hour (cmh) during welding. Table 2 lists the CSC-MIG welding process parameters used for the reported experiments.

The samples produced were transversely cut using a Buehler Delta AbrasiMet abrasive cutter, mounted in Bakelite, ground with several steps of progressively finer SiC paper and polished with diamond suspensions up to a 1 μm finish. Optical micrographs of cross sections were taken with a Nikon Epiphot 200 with Clemex JS2000 image analysis system. Scanning electron microscopy (SEM) examination was performed using a JEOL JSM-840A and a Hitachi S-4700. Electron backscattered diffraction (EBSD) mapping was performed using a Nordlys II camera and the HKL Channel 5 software. The acquisition parameters were an accelerating voltage of 15 kV, an 8 × 8 image binning, a dwell time of 20 ms and a step size of 30 nm.

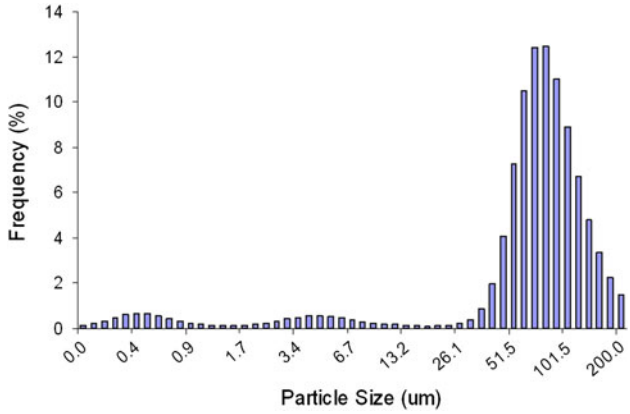

Fig. 1 Particle size distribution of the WC powder in the welding wire

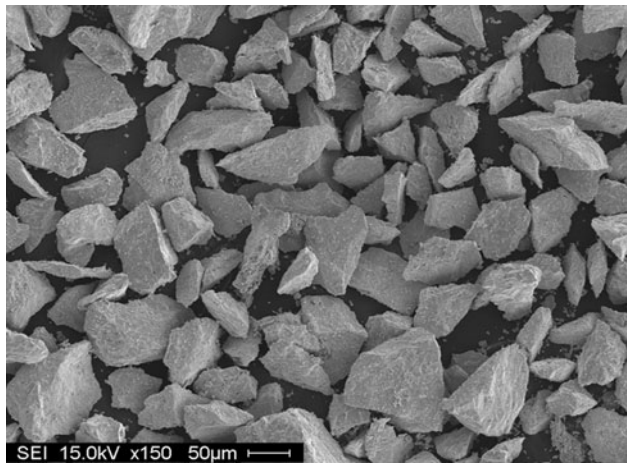

Fig. 2 Micrograph of WC powder in the welding wire

Table 2 CSC-MIG welding process parameters and energy input for the reported depositions

Sample	A	B	C	D	E	F
Heat input, J/mm	10.1	17.3	22.7	38.9	11.7	108.7
Current data						
Arc time						
Initial arc current, A	30	30	80	80	80	250
Time, ms	7	7	7	7	7	7
Mid arc current, A	30	100	80	160	80	250
Time, ms	7	7	7	7	7	7
End arc current, A	30	30	80	80	80	250
Short circuit time						
Start short current, A	20	20	40	40	40	200
Time, ms	7	7	7	7	7	7
Mid short current, A	20	20	40	40	40	200
Time, ms	7	7	7	7	7	7
End arc current, A	20	20	40	40	40	200
Ramp rates						
Rise, A/ms	200	200	200	200	200	200
Fall, A/ms	200	200	200	200	200	200
Wirefeed data						
Down wirefeed speed, mpm	5	5	8	6	6	12
Delay before wire down, ms	0	0	0	0	0	0
Up 1 wirefeed speed, mpm	5	5	5	5	2	5
Delay before wire up, ms	0	0	0	0	0	0
Up 2 wirefeed speed, mpm	7	7	7	7	15	7
Arc length, mm	0.5	0.5	0.5	0.5	0.2	0.5
Penetration delay, ms	6	6	6	6	5	6
Start sequence data						
Preflow time, s	0.5	0.5	0.5	0.5	0.5	0.5
Runin wirefeed speed, mpm	2	2	2	2	2	2
Process starting current, A	60	60	60	60	60	60
Initial arc length, mm	2	2	2	2	2	2
Preheat current, A	60	60	60	60	60	60
Preheat time-start delay, ms	50	50	50	50	50	50
Stop sequence data						
Stop arc length, mm	1.4	1.4	1.4	1.4	1.4	1.4
Stop time, ms	40	40	40	40	40	40
Arc stop current, A	40	40	40	40	40	40
Postflow time, s	0.3	0.3	0.3	0.3	0.3	0.3

No noise reduction technique was used. The phases used were Ni (space group: 225, a: 3.54 Å), WC (space group: 187, a: 2.91 Å, c: 2.84 Å), and W_2C (space group: 194, a: 2.98 Å, c: 4.71 Å). A Si(Li) detector and the Oxford Inca software were used for the energy dispersive spectroscopy (EDS) analysis. The acquisition parameters were an accelerating voltage of 15 kV, a processing time of 5 and a live time for the mapping of 2 h. A Bruker D8 Discovery diffractometer using cobalt K_α x-rays at 40 kV and 0.002° step size was used for collecting x-ray diffraction (XRD) patterns. Hardness measurements were taken on a Buehler 5114 macro-vickers.

3. Results and Discussion

3.1 Characterization of Welding Electrode

The cored electrode wire consisted of an outer sheath made of Ni and a filler powder composed of WC/Si/Fe/B as shown by XRD. Figure 3 shows the XRD pattern of the filler powder. From this, it can be seen that the tungsten carbide powder is composed of WC and W_2C. W_2C as a wear resistant material

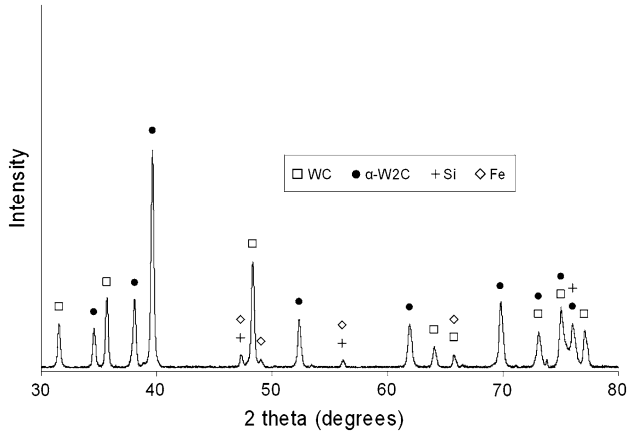

Fig. 3 XRD pattern of electrode wire filler powder

is undesirable as its mechanical properties are inferior to WC; it is more brittle and has been shown to exhibit lower chemical corrosion resistance (Ref 2, 11). The presence of W_2C in the stock powder depends on the manufacturing process, these unwanted carbides can be formed in the production of tungsten carbide (Ref 19, 20). Boron is used as an additive up to 25 at.% to reduce the melting point of the matrix, while silicon is added as it has been shown to visibly increase the self-fluxing ability of the alloy (Ref 21). When B and Si are added in conjunction with one another, they have been shown to deoxidize the substrate (Ref 21, 22).

3.2 CSC-MIG Welding Current Waveform

Three current and voltage waveforms used to produce coatings sample A, sample B, and sample E are illustrated in Fig. 4(a), (b), and (c), respectively, to demonstrate the variability in obtainable waveforms. A waveform of traditional MIG welding is illustrated in Fig. 4(d), for comparison purposes. The CSC system allows welding using a square waveform and has the capability to add a pulse in the short phase and/or the arc phase. The sample A waveform is a variation on the short-circuit welding waveform seen in traditional MIG welding. A pulse in the arc phase was added in the waveform of sample B. The addition of this pulse resulted in better fusion of the coating with the basemetal and increased the heat input from 10.1 to 17.3 J/mm. Research on pulsed GMAW (GMAW-P) has shown that when properly configured, the addition of a pulse has the effect of lowering the overall heat input during welding (Ref 23). In this case, the waveform for sample B was created to show the capabilities of the CSC system to add a pulse and was not configured to minimize the heat input. Sample E was created to demonstrate how the CSC system can control the duration of the short circuit and arc phases.

3.3 Macrostructure and Microstructure Analysis and Characterization

Two typical weldbead depositions are shown in Fig. 5; a low heat input weldment (10.1 J/mm) in Fig. 5(a) and a high heat input deposit (108.7 J/mm) in Fig. 5(b). Weldments are characterized by a continuous, uniform profile and are free from spatter. Initial analysis of the weldments surfaces shows transverse cracking. When welding with hardfacing materials,

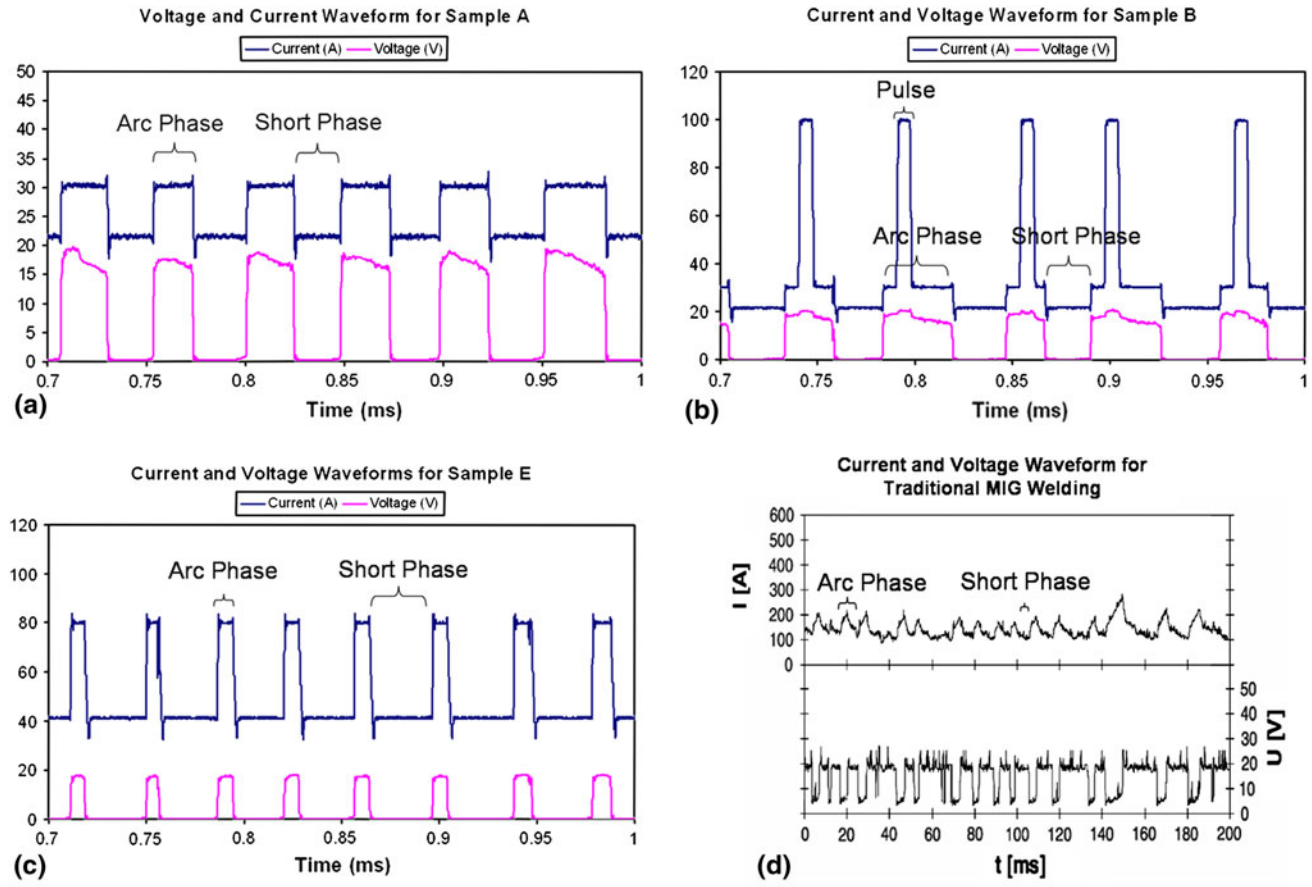

Fig. 4 Current and voltage waveform as a function of time for: (a) sample A having square waveform; (b) sample B having square waveform with the addition of a pulse in the arc-phase; (c) sample E having a lengthened time duration in the short-circuit phase and shortened duration in the arc-phase; (d) traditional MIG welding (Ref 18)

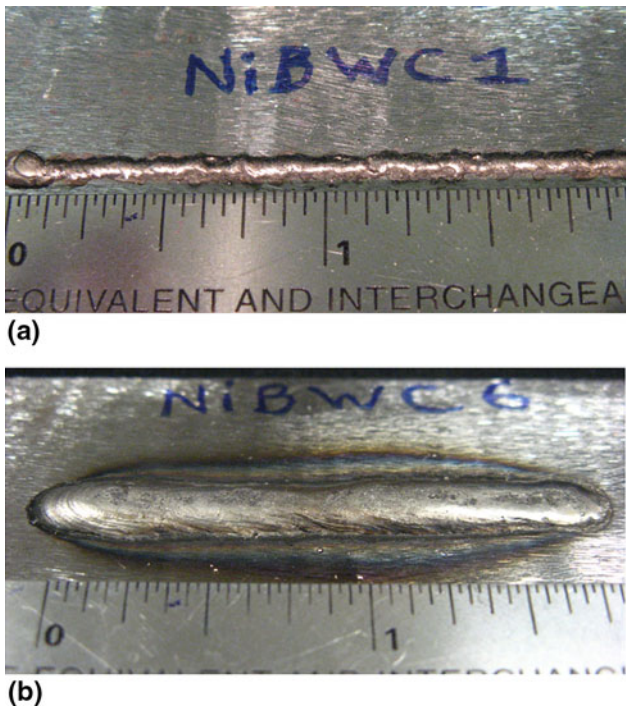

Fig. 5 Beads produced with the CSC-MIG welding system using (a) low heat input parameters—sample A and (b) high heat input parameters—sample F

cracking is to be expected. This is because of the high hardness and low ductility of the depositions which cannot accommodate the stresses generated during solidification and cooling (Ref 24). The presence of transverse cracking is likely to reduce the wear resistance of the coating as it is a point from which chipping and spalling can initiate.

Figure 6 shows the cross section of six depositions made with the parameters outlined in Table 2. All coatings were metallurgically bonded with the substrate material although the lowest heat input deposition (sample A) did exhibit a small amount of detachment from the basemetal. For this reason the heat input of sample A was considered as the lowest necessary to achieve adequate adhesion in these experiments. All depositions showed good dispersion of tungsten carbide throughout the matrix. Sample E contained 3.3% porosity while the remaining samples contained between 0.04 and 0.6 % porosity. Average porosity level for sample A to F was 0.75%.

The level of substrate dilution into the deposited coating can be defined as the ratio of the maximum depth of melted substrate to the sum of the maximum depth of melted substrate and maximum coating height (Ref 25). Samples A through E, with heat input range 10.1-38.9 J/mm, show minimal amounts of substrate dilution ($<5\%$). The highest heat input coating, sample F with 108.7 J/mm, shows dilution ratio between 35 and 40%. This is considered a high amount of dilution as the substrate material can cause a change in the material properties of the hardfacing. A dilution level of $<10\%$ has been proposed as acceptable levels for claddings (Ref 25).

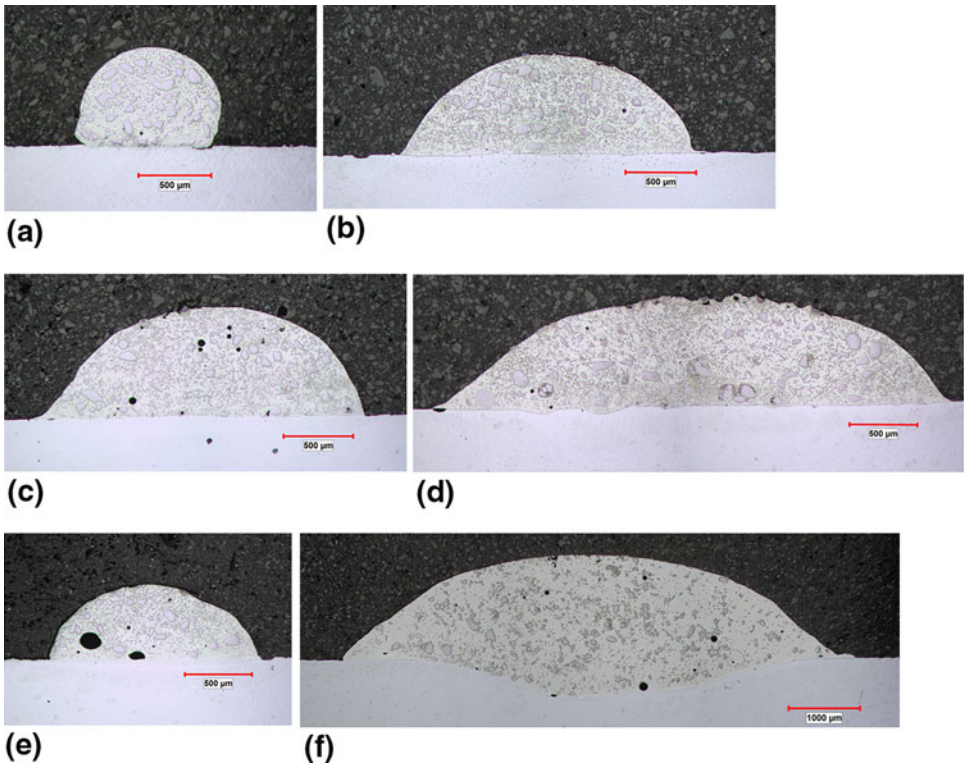

Fig. 6 Cross-sectional images of samples A to F. Hardfacings show good metallurgical bond with iron substrate and small amounts of porosity

The XRD patterns of samples A and F can be seen in Fig. 7(a) and (b), respectively. The phases corresponding to the x-ray diffraction patterns in the composite coatings are outlined in Table 3. Some iron-based compounds have been identified. Their presence originates from the reaction of the alloying elements with the 0.7% Fe present in the electrode wire filler powder and significant dilution of the iron substrate. Given the level of Fe present and the longer molten state dwell time seen in sample F, ternary phases in the Fe-W-C system are likely to form (Ref 26). This can explain the formation of the hexagonal η carbide, FeW_3C, in sample F which is not present in sample A.

Typical microstructure backscatter electron images for the low and high heat input depositions are shown in Fig. 8. Many authors have reported on the various phases that form between the WC and the alloying elements in the binder material (Ref 2, 27-29). The compounds formed are thought to depend on the composition of the alloy and the solidification process (Ref 27). In addition, the longer dwell time in the molten state, as is the case for the high heat input deposition, has been shown to accelerate the formation of carbides (Ref 26). In agreement with this, several morphological features characteristic of the high heat input deposition (Fig. 8b) are not present or are substantially less pervasive in the low heat input deposition (Fig. 8a). Two such features are the dendritic phase (marked as 1 in Fig. 8b) and the needle-shaped formations (marked as 2 in Fig. 8b) which can be seen throughout the matrix of sample F but not in sample A. A higher magnification image of the needle-shaped formation is shown in Fig. 8(d). Based on the XRD (Fig. 7b) and EDS analyses, these features are thought to be FeW_3C.

A two-phase system (marked as 3 in Fig. 8a and b, shown clearly in Fig. 8c) can be seen within the Ni matrix. As found

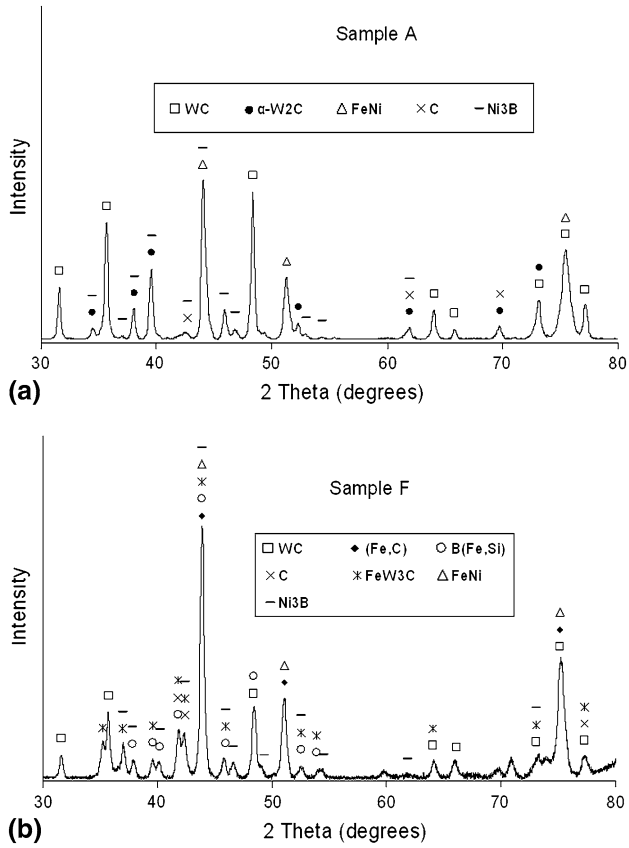

Fig. 7 X-ray diffraction spectrum of the low heat input—sample A (a) and high heat input—sample F (b) depositions

by XRD analysis and commonly identified in other Ni-based MMCs with WC as a reinforcing agent, the dark phase likely corresponds to FeNi or Ni_3B (Ref 2, 27, 28, 30, 31). The light colored phase is dendritic and, as a result of the slower cooling rate, larger arm spacing characterizes sample F as compared with sample A. Although there was only one W-based phase identified (FeW_3C) in either sample A or F, EDS analysis reveals that the lighter colored dendritic phase contains W. The W entered the matrix during the partial dissolution of the WC particles. The formation of a W-based phase is likely and consistent with the fact that molten Ni dissolves WC rapidly, facilitating the formation of Ni-W-C liquid alloys (Ref 9). It is possible that the W is forming a non-stoichiometric phase within the Ni matrix which causes a slight shift in position of the Ni peaks to lower Bragg angles.

In the starting tungsten carbide powder XRD (refer to Fig. 3) the W_2C:WC ratio for the two largest peaks is greater than two. After welding, the XRD of the low heat input deposition (Fig. 7a) reveals that the W_2C:WC peak ratio diminishes to one-half in sample A. The XRD of sample F (Fig. 7b) shows that the WC phase is less present in the high heat input deposition when compared with the low energy input deposition. The W_2C phase is not found in the high heat input deposition. The diminishment of the relative occurrence of W_2C in the depositions made using the CSC-MIG is the reverse behavior of that which is observed in HVOF coating systems. HVOF research shows that the W_2C:WC ratio increases with decarburization (Ref 32). The reduction in relative ratio of W_2C:WC with increasing heat input suggests that the CSC hardfacing process does not decarburize WC. On the other hand, a WC dissolution phenomenon is occurring.

Table 3 Potential phases in welding samples A and F based on x-ray diffraction data

Welding condition	Heat input, kJ/in	Possible phases present based on XRD
A	0.26	WC, α-W_2C, C, FeNi, Ni_3B
F	2.76	WC, (Fe,C), B(Fe,Si), C, FeW_3C, FeNi, Ni_3B

To investigate the dissolution of the WC particles during welding, EDS mapping and EBSD were employed. Figure 9 shows an elemental map of a WC particle within the Ni-based alloy matrix for sample E. Figure 9(b), (c), and (d) depicts the variations in C, Ni, and W, respectively. The mapping shown in Fig. 9(b) reveals that the core of the starting WC particles contains WC (darker phase) and W_2C (lighter phase), as depicted by the corresponding changes in C and W. A distinct reaction layer around the particles can be observed. Based on the mapping results, this layer seems to be composed of WC. To further infer the composition, EBSD was used to characterize the reaction layer. Figure 10(a) shows a SEM image of the area to be analyzed. Region marked A corresponds to the matrix; region B is the interfacial reaction layer; while the region C corresponds to the interior of the particle. Figure 10(b) shows the EBSD phase map of Ni (red), WC (blue), and W_2C (green). The core of the reinforcement is therefore composed of WC and W_2C while the reaction layer is indeed WC.

In order to explain the formation of the WC reaction layer around the WC/W_2C reinforcing phase, the W-C binary system and the Ni-W-C ternary phase diagrams have been analyzed.

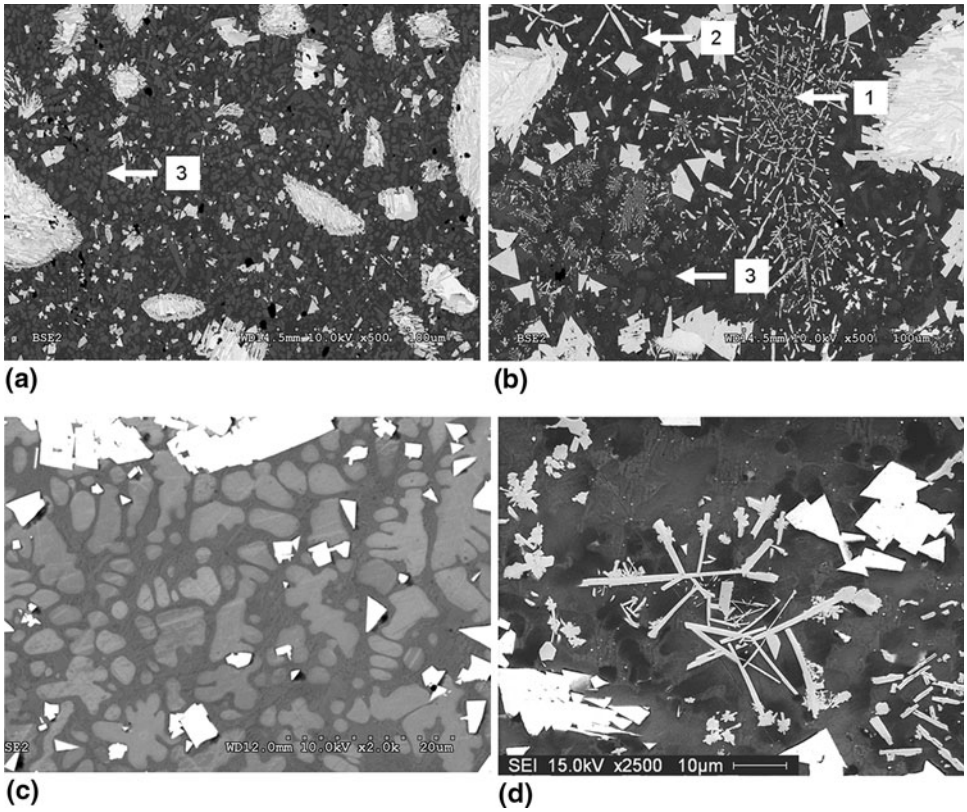

Fig. 8 Typical cross-sectional images of Ni-alloy-based hardfacings for low heat input (a) and high heat input (b) conditions. Higher magnification images clearly showing the two-phase system within the matrix (c) of sample A and a needle-like/lamellar carbide (d) in sample F

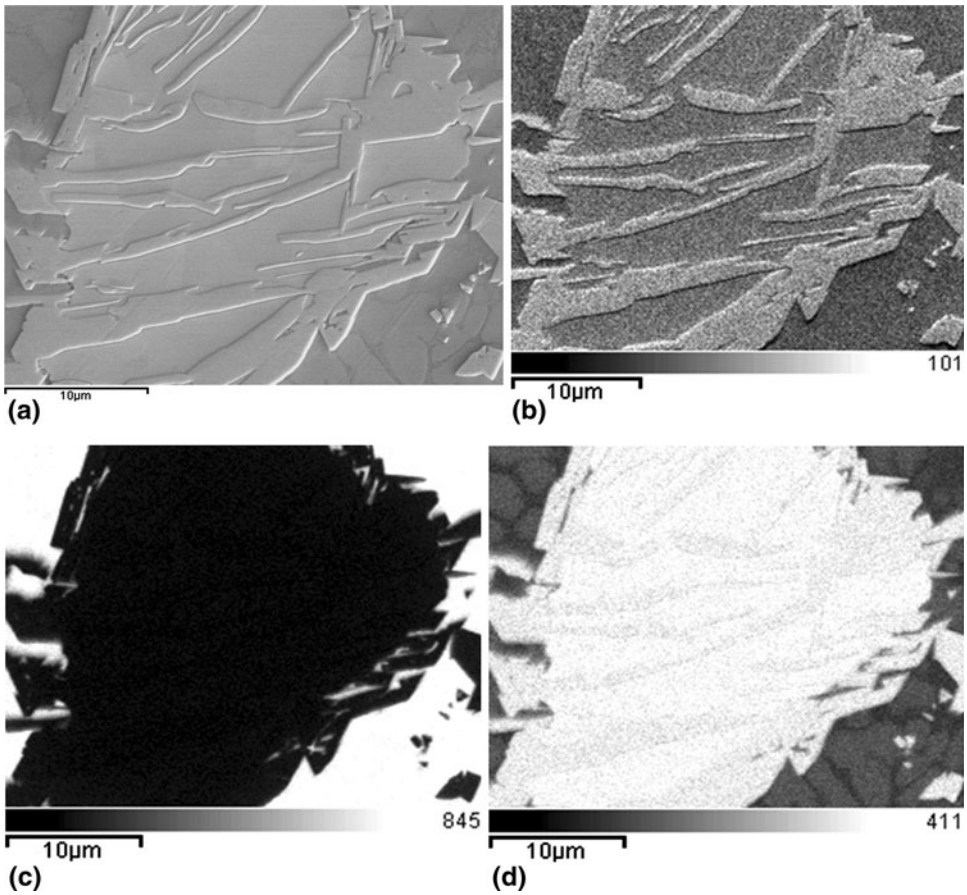

Fig. 9 EDS mapping of Ni, C, and W content in and around a tungsten carbide particle. The micrographs correspond to (a) secondary electron image of WC/W_2C particle; (b) the variation of C content; (c) the variation of Ni content; and (d) the variation of W content

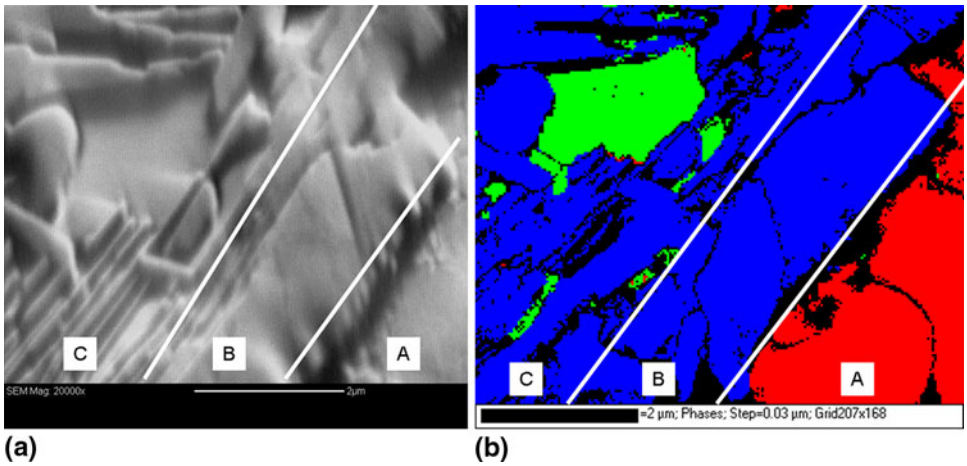

Fig. 10 (a) Secondary electron SEM image taken at 15 kV of the interface region between a WC/W_2C particle and the matrix for identification by EBSD; (b) EBSD map of the phases present in the interface region. Three distinct phases can be seen: red represents the Ni matrix [A], blue represents the WC [B], and green represents the W_2C [C] (Color figure online)

Given that welding is characterized by very high heating and cooling rates it cannot therefore be considered as an equilibrium process. Despite this fact, the phase transformations occurring can be better understood by considering the interactions between the main constituent elements of the weld pool at equilibrium conditions. A representative value for the droplet temperature in open arc welding deposition techniques, such as pulsed or spray transfer, has been established at 2400 °C (Ref 33). Although short-circuit welding techniques have significantly lower droplet temperatures, a maximum weld pool temperature (peak temperature) of 2400 °C has been used for the calculation of the ternary system using FactSage™ software. At the maximum weld pool temperature, the ternary phase diagram can be divided into two segments; a carbon-rich

and a carbon-deficient segment. The carbon-deficient segment contains two and three phase fields where γ-Ni is in equilibrium with W_2C and/or η carbides. Although Gustafson and Ansara (Ref 34) did not include $M_{12}C$ carbide in his evaluation because they were not found to participate in solid/liquid equilibrium, $(Ni,W)_6C$- and $(Ni,W)_{12}C$-type carbides with FCC crystal structure have been reported to precipitate on solidification of the melt (Ref 2, 35). The carbon-rich segment is divided into three sections. With low concentration of W and C, γ-Ni alloy is in equilibrium. As the concentrations of W and C increase, two-phase field γ-Ni + $C_{(graphite)}$ and three-phase field γ-Ni + $C_{(graphite)}$ + WC become thermodynamically stable. Given that WC and W_2C have low enthalpies of formation ($\Delta H_f°(WC) = -42.3 \pm 0.8$ kJ/mol, $T < 1575$ K and $\Delta H_f°(W_2C) = -30.5 \pm 1.3$ kJ/mol, $T > 1575$ K), WC and W_2C easily dissolve in the Ni-based weld pool (Ref 36). Melting of the electrode wire followed by the dissolution of WC/W_2C reinforcing phase forms a Ni-based alloy solvent with low concentration of W and C solute. Mass transport of dissolved elements through fluid flow and short distance liquid phase diffusion produces a homogeneous distribution of W and C atoms in the matrix (Ref 2). The XRD database used for peak analysis does not include any of the η carbides, however, referring to the XRD spectrum of Zhou et al. (Ref 28, 35) the peaks for M_6C- and $M_{12}C$-type carbides align with the peaks from the XRD spectrum of samples A and F. It is therefore likely that upon solidification of the carbon-deficient melt, η carbides are precipitated. Initial precipitation of M_6C- and $M_{12}C$-type carbide shifts the carbon concentration to the carbon-rich side of the Ni-W-C phase diagram. As the melt cools from peak temperature through final solidification in the C-rich segment, there is precipitation of stable and metastable phases most of which are alloyed with Si, B, Fe found in the weld pool. At temperatures around 2000 °C, γ-Ni + $C_{(graphite)}$ + WC is likely precipitated, followed by γ-Ni + WC (at 1500 °C) which is subsequently followed by Ni + $C_{(graphite)}$ + WC (at 1000 °C). It is suggested that the edges of the WC/W_2C reinforcing phase act as nucleation sites onto which the WC reaction layer heterogeneous precipitates during cooling of the weld pool. The continuity of the texture between the core particle and reaction layer shows evidence that the WC layer is produced by epitaxial precipitation.

3.4 Quantification of the Tungsten Carbide Dissolution

Analysis of the tungsten carbide particle size distribution was performed prior to and after welding. This was achieved using a powder characterization technique which uses the projected area of the cross section of a particle to determine the equivalent diameter of a sphere having cross-sectional area equal to the projected area. The equivalent spherical particle size diameter distributions for the stock WC powder compared with samples A and F are shown in Fig. 11. As illustrated, the particle size distributions for samples A and F have significantly shifted toward smaller particle sizes when compared to the starting WC feedstock. The high heat input on sample F and low heat input to sample A seemed to have no significant influence on the final particle size distribution. The statistical analysis of these distributions provides the results shown in Table 4. Using the equivalent spherical particle size diameter powder characterization technique, the stock tungsten carbide powder was determined to have an average particle diameter size of 99 μm with D_{50} = 95 μm. After welding, the average particle diameter dropped to 43 μm for both samples A and F. This reduction in average particle diameter was mirrored by the D_{50} values corresponding to 27 μm for sample A and 36 μm for sample F. The significant drop in average particle size and D_{50} is attributed to the dissolution phenomenon of the WC particles into the liquid matrix during welding. Another

Table 4 Statistical analysis of stock tungsten carbide powder and coating samples A and F

Sample	Average, μm	D_{10}, μm	D_{50}, μm	D_{90}, μm	S_w, μm/μm
Starting WC powder	99	58	95	143	6.53
A	43	13	27	90	3.05
F	43	18	36	83	3.86

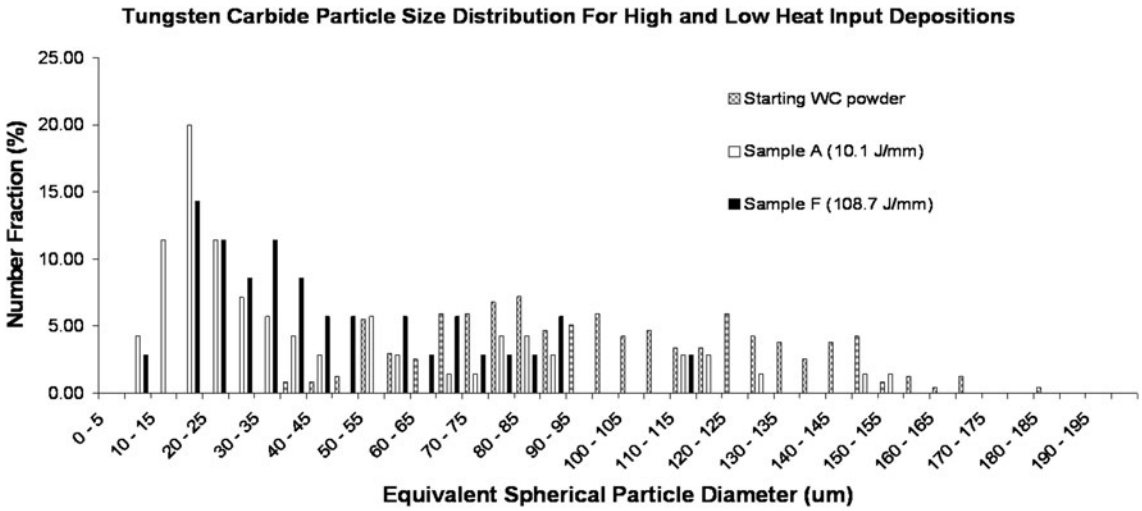

Fig. 11 Graphical illustration of the particle size distributions for the starting WC powder before welding and for the high and low heat input conditions after welding

statistical approach for comparison of the WC particles before and after welding is the size distribution width, S_w. A high S_w value represents a narrow distribution while a low S_w value represents a wide spread of the particle size distribution. For WC, the S_w has a significantly lower value after welding. Prior to welding, the S_w for the WC particles was 6.5. After welding, the S_w decreased to 3 for sample A and 3.9 for sample F. The widening of the size distribution is again attributed to the thermal decomposition of WC particles. The largest WC particles—which have a relatively small surface area to volume ratio, remain large despite the heat input. On the other hand, most WC particles suffer significant dissolution which causes a shift in the particle size distribution to smaller particle diameters. The combination of the large particles largely unaffected by heat and the reduction in size of the smaller particles has the effect of widening the overall particle size distribution or lowering the value of S_w.

Carbide dissolution is occurring during welding despite the fact that the CSC-MIG process has inherently lower heat input when compared with the conventional MIG process. The volume fraction of the WC coverage after welding was calculated by image analysis and the results indicate that the level of dilution increases with energy input. Comparing the extreme conditions, the low heat input, sample A, has a $25.2 \pm 1.22\%$ volume fraction of reinforcing particles, while the high heat input, sample F, has a volume fraction reduced to $14.5 \pm 0.56\%$. The values obtained for the volume fraction of WC serve as an indication of the amount of tungsten carbide coverage in the coating. However, variation in the quantity of tungsten carbide per length of electrode wire is to be expected in the manufacturing process. It is for this reason that the standard deviation of the volume fraction can easily fluctuate from one cross section to another. A summary of the evolution of the volume fraction of WC particles is presented in Fig. 12.

3.5 Quantification of the Reaction Layer Formation Around the WC Particles

As demonstrated in section 3.3, a WC layer formed around the reinforcing particles. For each sample, the layer was analyzed for thickness, thickness distribution, and thickness distribution width (S_w). Figure 13 shows the effect of adding a pulse on the reaction layer thickness for the low energy input deposition. The addition of the pulse shifted the thickness of the reaction layer from an average value of 3.8 to 4.6 μm. A similar trend can be seen with the medium heat input deposition with a pulse (sample D) and without a pulse (sample C). The pulse slightly shifted the average value from 4.3 to 4.9 μm. Thus, it can be seen that the addition of a pulse slightly increases the reaction layer thickness for the same base waveform. In addition, a significant difference in the reaction layer thickness is found between the high and the low heat input depositions. The extra 98.6 J/mm input to sample F shifted the average reaction layer thickness from 3.8 to 7.6 μm. The results indicate that the thickness of the WC reaction layer between the reinforcing phase and the matrix is more influenced by the energy input than by the presence of a pulse in the arc phase. In WC reinforced composite coatings, the carbide/matrix interface layer is partly responsible for the adhesion of the carbides to the matrix and influences the mechanical properties of the coating (Ref 22, 27, 37, 38). Research suggests the reaction layer produces a higher bonding strength between the WC particles and the Ni matrix and thus produces a coating with greater wear resistance (Ref 22, 27). Although the reaction layer thickness increases with energy input, a larger reaction layer will not always produce a more wear resistant hardfacing. As the energy input during welding increases, other competing factors such as carbide thermal decomposition as well as basemetal dilution may lead to a reduction of the wear resistance (Ref 27). Appropriate parameter selection is needed to establish a balance between competing phenomena.

3.6 Quantification of the Newly Formed WC Particles

The newly formed WC particles precipitated in the Ni-based alloy matrix have been investigated by EBSD and analyzed for average size. These particles are important as they are a direct by-product of the dissolution of the original reinforcing phase. The EBSD experiments reveal that the newly formed WC particles are single crystals. SEM images of the original and precipitated particles can be seen in Fig. 14. The average equivalent spherical particle diameter distribution of the newly formed WC particles for several hardfacings can be seen in Fig. 13. The data show no definite trends between the low heat input non-pulsed and pulsed waveforms or the medium heat input non-pulsed and pulsed depositions. This is likely due the similar quantity of WC particle dissolved during the welding for the low and the medium energy input (see also Fig. 12). On the other hand, a notable size difference between newly formed WC particles for the high heat input and low heat input hardfacings is observed. The average particle size increased nearly three times from 2.5 to 7.2 μm. The increasing size of the particles is thought to be attributed to the higher quantity of WC dissolved and associated with the longer duration of the

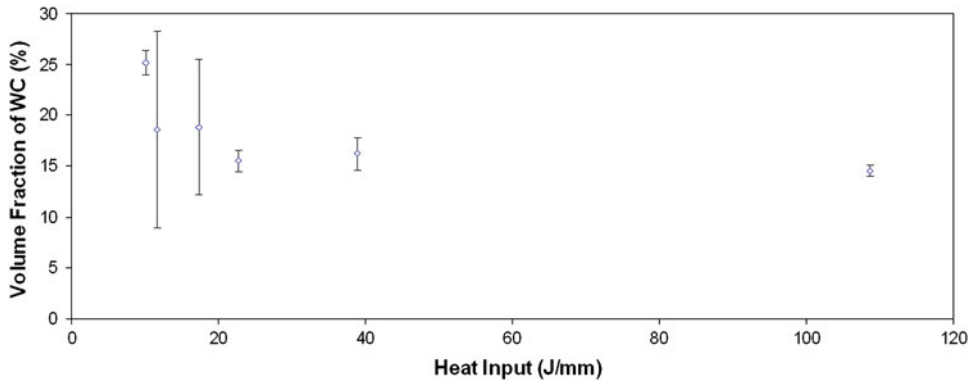

Fig. 12 Volume fraction of tungsten carbide with heat input for samples A to F

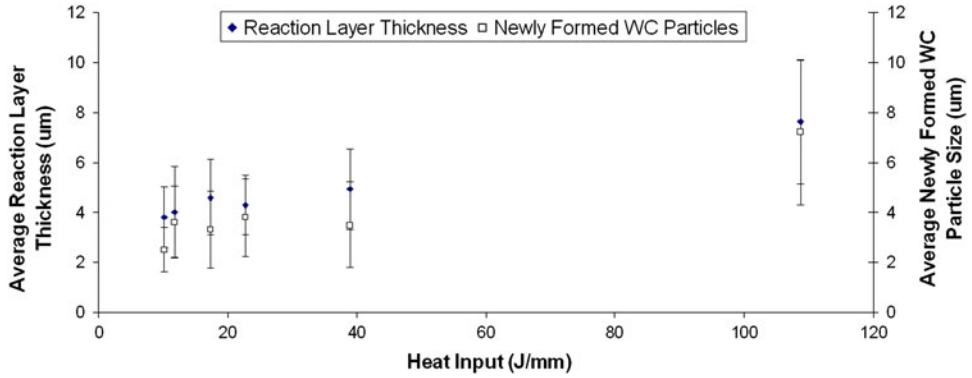

Fig. 13 The effect of heat input on the WC layer thickness and size of newly formed WC particles

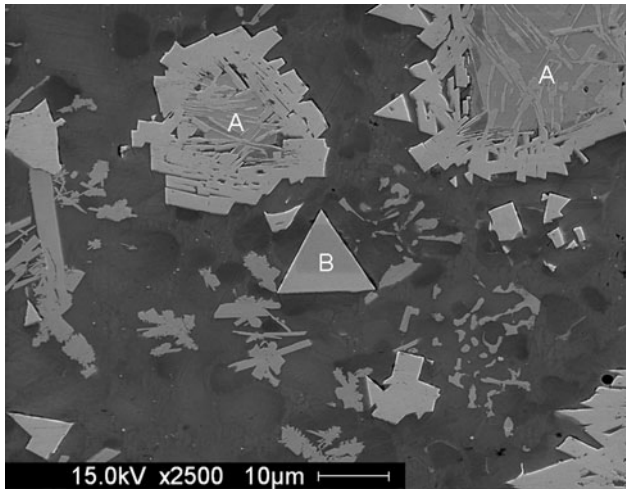

Fig. 14 Backscatter electron images showing the original WC/W_2C particles with precipitated reaction layer (marked A) and the morphology of the newly formed WC particles (marked B)

liquid melt pool. This could help in the formation of larger clusters in the liquid matrix that would reprecipitate as larger newly formed WC particles.

3.7 Hardness of Weldments

Microstructural features, surface composition, and hardness are three principal factors which affect material wear properties (Ref 39). The easiest to measure yet most indicative property of wear resistance is surface hardness and, as a general rule, the higher the hardness the higher the wear resistance (Ref 8, 39, 40). For the measurement of surface hardness for materials with reinforcing particles, it is important to consider that the value obtained varies significantly with the fraction of reinforcing carbide to matrix ratio contained under the indent surface (Ref 41). It is important to choose an indent force that, as much as possible, contains a representative proportion of matrix to reinforcing particle. The surface hardness of the low heat input coating, sample A, was 587 HV_{10} while that of the high heat input coating, sample F, was 410 HV_{10}. The hardness measurements for samples A to F seem to indicate that the higher the heat input during deposition, the lower the hardness of the coating. The reduction in hardness with heat input can be attributed to several factors. Although there is precipitation of a shell of WC around the reinforcing particles that increases with heat input, it is a function of the rate of dissolution of the WC/W_2C carbides. The potential benefits gained by the WC reaction layer are offset by the high levels of dilution. The dissolution of WC/W_2C particles creates large distances between the reinforcing phases therefore exposing more of the soft matrix to the indenter. Another factor affecting the hardness measurements is the increasing level of Fe intermixing from basemetal dilution with energy input during welding. It is probable that the increasing level of Fe mixing with the matrix has a great impact on the hardness of the coatings (Ref 41). Furthermore, a longer dwell time in the molten state accelerates the formation of secondary and brittle carbides. Figure 15 shows the hardness of coating samples A through F.

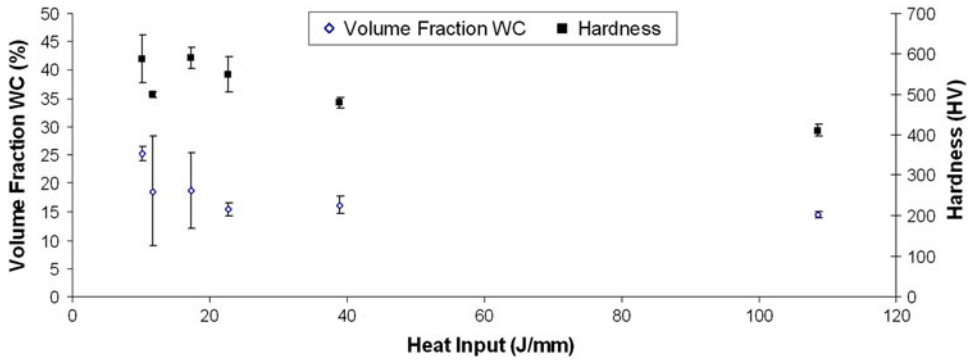

Fig. 15 Effect of heat input on the volume fraction and hardness for samples deposited by CSC-MIG

4. Conclusions

A commercially available WC/Ni hardfacing electrode wire was deposited by controlled short-circuit (CSC)-MIG welding system. The microstructure of several hardfacings with different welding parameters and heat inputs was analyzed. Analysis of the welding system and deposited coatings resulted in the following conclusions:

- The CSC-MIG welding system successfully deposited WC/Ni coatings using a hardfacing electrode wire.
- The CSC-MIG welding system can deposit continuous beads free from spatter with 0.75% average porosity on a carbon steel substrate. Transverse cracking is present.
- The CSC-MIG allows for a high degree of user control over the current waveform and is characterized by heat inputs that are an order of magnitude lower than traditional MIG welding. Heat input for the analyzed coatings ranged from 10.1 to 108.7 J/mm.
- Many phases and compounds are formed in the weld pool. Phases identified in the hardfacings were: WC, α-W_2C, FeNi, FeW_3C, C, (Fe,C) Ni_3B, and $B(Fe,Si)_3$.
- The detrimental decarburization reactions seen in HVOF thermal spraying do not occur with the CSC-MIG welding system.
- The formation of a shell of WC was identified around the mixed WC/W_2C reinforcing phase after welding. The thickness of this shell increased with welding energy from 3.8 to 7.2 μm for the low and high heat input conditions, respectively. Isothermal Ni-W-C ternary phase diagrams were used to propose a mechanism for the precipitation of this layer.
- The size distributions of ceramic particles after welding were similar for high and low heat input coatings. The level of WC dissolution increased significantly with heat input.
- Newly formed WC particles were precipitated in the Ni-based alloy matrix. Their size distribution increased from D_{50} of 2.4 μm in the low heat input weldment to 6.75 μm in the high heat input weldment.
- The hardness of the deposited coatings decreased from 587 HV_{10} to 410 HV_{10} when the energy input was increased from 10.1 to 108.7 J/mm.

Acknowledgments

The authors would like to thank NSERC and McGill University for the overall funding of the study. The authors would like to thank Professor In-ho Jung for his help with FactSage and Dr. Pierre Hovington from Hydro-Québec for the help with the EBSD and EDS acquisitions. Finally, the authors would like to thank Polymet for the supply of the WC-based welding wire.

References

1. G.V.H.J. Scussel, *ASM Handbook—Friction and Wear of Cemented Carbides*, Vol 18, ASM International, 1992
2. Q. Li, T.C. Lei, and W.Z. Chen, Microstructural Characterization of WCp Reinforced Ni-Cr-B-Si-C Composite Coatings, *Surf. Coat. Technol.*, 1999, **114**, p 285–291
3. J. Przybylowicz and J. Kusinski, Structure of Laser Cladded Tungsten Carbide Composite Coatings, *J. Mater. Process. Technol.*, 2001, **109**, p 154–160
4. R.S. Lima, J. Karthikeyan, C.M. Kay, J. Lindemann, and C.C. Berndt, Microstructural Characteristics of Cold-Sprayed Nanostructured WC-Co Coatings, *Thin Solid Films*, 2002, **416**, p 129–135
5. A. Neville, F. Reza, S. Chiovelli, and T. Revega, Erosion-Corrosion Behaviour of WC-Based MMCs in Liquid-Solid Slurries, *Wear*, 2005, **259**, p 181–195
6. J. Nurminen, J. Näkki, and P. Vuoristo, Microstructure and Properties of Hard and Wear Resistant MMC Coatings Deposited by Laser Cladding, *Int. J. Refract Metal Hard Mater.*, 2009, **27**, p 472–478
7. H. Chen, C. Xu, J. Qu, I.M. Hutchings, P.H. Shipway, and J. Liu, Sliding Wear Behaviour of Laser Clad Coatings Based Upon a Nickel-Based Self-Fluxing Alloy Co-Deposited with Conventional and Nanostructured Tungsten Carbide-Cobalt Hardmetals, *Wear*, 2005, **259**, p 801–806
8. N.Y. Sari and M. Yilmaz, Improvement of Wear Resistance of Wire Drawing Rolls with Cr-Ni-B-Si+WC Thermal Spraying Powders, *Surf. Coat. Technol.*, 2008, **202**, p 3136–3141
9. J.M. Guilemany, J. Nutting, J.R. Miguel, and Z. Dong, Microstructure Characterization of WC-Ni Coatings Obtained by HVOF Thermal Spraying, *Scripta Metall. Mater.*, 1995, **33**, p 55–61
10. Q. Wang, Z.H. Chen, and Z.X. Ding, Performance of Abrasive Wear of WC-12Co Coatings Sprayed by HVOF, *Tribol. Int.*, 2009, **42**, p 1046–1051
11. J. Guilemany, J. de Paco, J. Miguel, and J. Nutting, Characterization of the W2C Phase Formed During the High Velocity Oxygen Fuel Spraying of a WC+12 pct Co Powder, *Metall. Mater. Trans. A*, 1999, **30**, p 1913–1921
12. Y. Qiao, T.E. Fischer, and A. Dent, The Effects of Fuel Chemistry and Feedstock Powder Structure on the Mechanical and Tribological Properties of HVOF Thermal-Sprayed WC-Co Coatings with Very Fine Structures, *Surf. Coat. Technol.*, 2003, **172**, p 24–41
13. R.W.S.R. Knight, *ASM Handbook—Thermal Spray Forming of Materials*, Vol 7, ASM International, 1998
14. G. Huismann, Direct Control of the Material Transfer: The Controlled Short Circuiting (CSC)-MIG Process, *Proceedings of the Gas Metal Arc Welding for 21st Century Conference* (American Welding Society), 6–8 December 2000, p 165–172
15. D.H.A. Joseph, D.F. Farson, and R. Richardson, Measurement and Calculation of Arc Power and Heat Transfer Efficiency in Pulsed Gas Metal Arc Welding, *Sci. Technol. Weld. Join.*, 2003, **8**, p 400–406
16. A. Joseph, D. Farson, D. Harwig, and R. Richardson, Influence of GMAW-P Current Waveforms on Heat Input and Weld Bead Shape, *Sci. Technol. Weld. Join.*, 2005, **10**, p 311–318
17. M.R. Bosworth, Effective Heat Input in Pulsed Current Gas Metal Arc-Welding with Solid Wire Electrodes, *Weld. J.*, 1991, **70**, p S111–S117
18. M. Suban and J. Tusek, Methods for the Determination of Arc Stability, *J. Mater. Process. Technol.*, 2003, **143–144**, p 430–437
19. M. Miyaki, Process for the Production of Tungsten Carbide or Mixed Metal Carbides, U. S. Patent, 1977
20. C.J. Terry, Macrocrystalline Tungsten Monocarbide Carbide Powder and Process for Producing, U.S. Patent, 1989
21. I.C. Grigorescu, C. Di Rauso, R. Drira-Halouani, B. Lavelle, R. Di Giampaolo, and J. Lira, "Phase characterization in Ni alloy-hard carbide composites for fused coatings", *Surf. Coat. Technol.*, 1995, **76–77**, p 494–498
22. M.J. Tobar, C. Álvarez, J.M. Amado, G. Rodríguez, and A. Yáñez, Morphology and Characterization of Laser Clad Composite NiCrBSi-WC Coatings on Stainless Steel, *Surf. Coat. Technol.*, 2006, **200**, p 6313–6317
23. P.K. Palani and N. Murugan, Selection of Parameters of Pulsed Current Gas Metal Arc Welding, *J. Mater. Process. Technol.*, 2006, **172**, p 1–10
24. A. Scotti and L.A. Albuquerque Rosa, Influence of Oscillation Parameters on Crack Formation in Automatic Fe-B Hardfacing, *J. Mater. Process. Technol.*, 1997, **65**, p 272–280
25. G. Abbas and D.R.F. West, Laser Surface Cladding of Stellite and Stellite-SiC Composite Deposits for Enhanced Hardness and Wear, *Wear*, 1991, **143**, p 353–363
26. O. Knotek, H. Reimann, and P. Lohage, Reactions Between NiCrBSi Matrixes and Carbide Additives in Coatings During Treatment, *Thin Solid Films*, 1981, **83**, p 361–367

27. S.-P. Lu and O.-Y. Kwon, Microstructure and Bonding Strength of WC Reinforced Ni-Base Alloy Brazed Composite Coating, *Surf. Coat. Technol.*, 2002, **153**, p 40–48
28. S. Zhou, Y. Huang, X. Zeng, and Q. Hu, Microstructure Characteristics of Ni-Based WC Composite Coatings by Laser Induction Hybrid Rapid Cladding, *Mater. Sci. Eng. A*, 2008, **480**, p 564–572
29. E.A. Levashov, E.S. Mishina, O.V. Malochkin, D.V. Shtansky, J.J. Moore, and M.I. Fadeev, Structure and Properties of Dispersion-Strengthened-with-Nanosized Particles Refractory Hard Material TiC-Ni-Alloy, *Sci. Technol. Adv. Mater.*, 2003, **4**, p 221–228
30. S.W. Huang, D. Nolan, and M. Brandt, Pre-placed WC/Ni Clad Layers Produced with a Pulsed Nd:YAG Laser Via Optical Fibres, *Surf. Coat. Technol.*, 2003, **165**, p 26–34
31. S. Zhou, X. Zeng, Q. Hu, and Y. Huang, Analysis of Crack Behavior for Ni-Based WC Composite Coatings by Laser Cladding and Crack-Free Realization, *Appl. Surf. Sci.*, 2008, **255**, p 1646–1653
32. J.M. Guilemany, S. Dosta, J. Nin, and J.R. Miguel, Study of the Properties of WC-Co Nanostructured Coatings Sprayed by High-Velocity Oxyfuel, *J. Therm. Spray Tech.*, 2005, **14**, p 405–413
33. G. Huismann and H. Hoffmeister, Control of the Short Circuiting MIG-Process Under Hyperbaric Conditions, *OMAE*, 1998
34. A.G.P. Gustafson and I. Ansara, A Thermodynamic Evaluation of the C-NI-W System, *Z. Metallkd.*, 1987, **78**(2), p 151–156. http://apps.isiknowledge.com/full_record.do?product=WOS&search_mode=GeneralSearch&qid=14&SID=4ABHIph1daOaJkhL@JB&page=1&doc=5
35. S. Zhou and X. Dai, Laser Induction Hybrid Rapid Cladding of WC Particles Reinforced NiCrBSi Composite Coatings, *Appl. Surf. Sci.*, 2010, **256**(14), p 4708–4714
36. D. Gupta and L. Seigle, Free energies of Formation of WC and W2C, and the Thermodynamic Properties of Carbon in Solid Tungsten, *Metall. Mater. Trans. A*, 1975, **6**, p 1939–1944
37. C. Just, E. Badisch, and J. Wosik, Influence of Welding Current on Carbide/Matrix Interface Properties in MMCs, *J. Mater. Process. Technol*, 2010, **210**, p 408–414
38. S.-P. Lu, O.-Y. Kwon, and Y. Guo, Wear Behavior of Brazed WC/NiCrBSi(Co) Composite Coatings, *Wear*, 2003, **254**, p 421–428
39. R. Chattopadhyay, *Surface Wear: Analysis Treatment and Prevention*, ASM International, Materials Park, OH, 2001
40. K. Van Acker, D. Vanhoyweghen, R. Persoons, and J. Vangrunderbeek, Influence of Tungsten Carbide Particle Size and Distribution on the Wear Resistance of Laser Clad WC/Ni Coatings, *Wear*, 2005, **258**, p 194–202
41. E. Badisch and M. Kirchgaßner, Influence of Welding Parameters on Microstructure and Wear Behaviour of a Typical NiCrBSi Hardfacing Alloy Reinforced with Tungsten Carbide, *Surf. Coat. Technol.*, 2008, **202**, p 6016–6022